PNAS RESEARCH ARTICLE | BIOCHEMISTRY

Conformational changes in the Niemann–Pick type C1 protein NCR1 drive sterol translocation

Kelly M. Frain[a,1], Emil Dedic[a,1], Lynette Nel[a,1], Anastasiia Bohush[a,b], Esben Olesen[a], Katja Thaysen[c], Daniel Wüstner[c], David L. Stokes[d,2], and Bjørn Panyella Pedersen[a,2]

Edited by Olga Boudker, Weill Cornell Medicine, New York, NY; received September 8, 2023; accepted February 22, 2024

The membrane protein Niemann–Pick type C1 (NPC1, named NCR1 in yeast) is central to sterol homeostasis in eukaryotes. *Saccharomyces cerevisiae* NCR1 is localized to the vacuolar membrane, where it is suggested to carry sterols across the protective glycocalyx and deposit them into the vacuolar membrane. However, documentation of a vacuolar glycocalyx in fungi is lacking, and the mechanism for sterol translocation has remained unclear. Here, we provide evidence supporting the presence of a glycocalyx in isolated *S. cerevisiae* vacuoles and report four cryo-EM structures of NCR1 in two distinct conformations, named tense and relaxed. These two conformations illustrate the movement of sterols through a tunnel formed by the luminal domains, thus bypassing the barrier presented by the glycocalyx. Based on these structures and on comparison with other members of the Resistance–Nodulation–Division (RND) superfamily, we propose a transport model that links changes in the luminal domains with a cycle of protonation and deprotonation within the transmembrane region of the protein. Our model suggests that NPC proteins work by a generalized RND mechanism where the proton motive force drives conformational changes in the transmembrane domains that are allosterically coupled to luminal/extracellular domains to promote sterol transport.

sterol uptake | Niemann–Pick type C protein | vacuole | cryo-EM | glycocalyx

Significance

Niemann–Pick type C1 (NPC1, named NCR1 in yeast) proteins play a critical role in sterol homeostasis by facilitating the integration of sterols into membranes of acidic organelles like lysosomes and vacuoles. The inner surface of these organelles' membranes is shielded by the glycocalyx. Here, we provide evidence that a glycocalyx is present in vacuoles from *Saccharomyces cerevisiae* and characterize conformational changes in NCR1 that we believe are responsible for the transport of sterols. Specifically, our structures suggest a transport model where sterol translocation is linked to proton-driven changes in the transmembrane region. This work clarifies how NPC proteins function and has broad implications both for lysosomal storage disorders and for mechanisms employed by the Resistance–Nodulation–Division superfamily.

Niemann–Pick type C1 (NPC1) membrane proteins are critical for establishing cell sterol homeostasis in eukaryotes. After uptake, sterols are transported via the endocytic pathway to acidic organelles (lysosomes and vacuoles) before integration via NPC proteins into the membrane for further redistribution in the cell (1). Failure to integrate sterols into the membrane leads to lipid accumulation in lysosomes and, in humans, gives rise to a neurodegenerative lysosomal storage disorder called NPC disease (2, 3). The *Saccharomyces cerevisiae* ortholog, named NCR1, has been used as a model system to understand NPC disease and mechanisms associated with sterol uptake in general (1, 4–7).

A central role of NCR1 and NPC1 is proposed to be the transport of sterols across the glycocalyx, a polysaccharide coating that maintains the integrity of the vacuolar/lysosomal membrane (Fig. 1*A*). The presence of a glycocalyx is well documented in the mammalian lysosome, although direct evidence for it in the vacuole, the fungal equivalent of the lysosome, is lacking (8–10). Nevertheless, three steps have been delineated for the membrane integration of sterols by NPC proteins: loading, transfer, and transport (1). Loading refers to the delivery of sterol to a luminal N-terminal domain (NTD) of NCR1. Thereafter, sterol is transferred from the NTD binding pocket into a ~60 Å long tunnel that traverses the glycocalyx. Transport refers to the movement of sterols through this tunnel, which is formed at the interface between a middle luminal domain (MLD) and a C-terminal domain (CTD) (Fig. 1*B*) (7, 11, 12). The membrane domain has 13 transmembrane helices (M1–M13) divided into the sterol-sensing domain (SSD, M2–M7) and the pseudo-SSD (pSSD, M8–M13). The SSD contains a gate at the end of the tunnel through which sterol is released into the luminal leaflet of the membrane after transport (1, 7, 11, 12). Two-fold pseudosymmetry relates the SSD to the pSSD and the MLD to the CTD (Fig. 1*B*).

NCR1 belongs to the Resistance–Nodulation–Division (RND) superfamily (13). The RND superfamily contains nine families that are widespread in prokaryotes and eukaryotes and that transport a variety of compounds (14). Most RND family members are not "transporters" in the conventional sense because these proteins do not move substrate from one side of the membrane to the other, but rather insert or extract substrate from the membrane or periplasmic space (14). This process is best characterized by the multidrug efflux pump, acriflavine resistance protein B (AcrB), which couples substrate transport through a porter domain (equivalent to the MLD and CTD of NCR1) to the proton motive force (13, 15). This energy coupling is mediated by a network of titratable residues at the point of pseudosymmetry between the SSD and pSSD, and this location has been

Author contributions: D.L.S. and B.P.P. designed research; K.M.F., E.D., L.N., A.B., E.O., and K.T. performed research; K.M.F., E.D., L.N., D.W., D.L.S., and B.P.P. analyzed data; and K.M.F., L.N., D.L.S., and B.P.P. wrote the paper.

The authors declare no competing interest.

This article is a PNAS Direct Submission.

[1]K.M.F., E.D., and L.N. contributed equally to this work.

[2]To whom correspondence may be addressed. Email: stokes@nyu.edu or bpp@mbg.au.dk.

This article contains supporting information online at https://www.pnas.org/lookup/suppl/doi:10.1073/pnas.2315575121/-/DCSupplemental.

Published April 3, 2024.

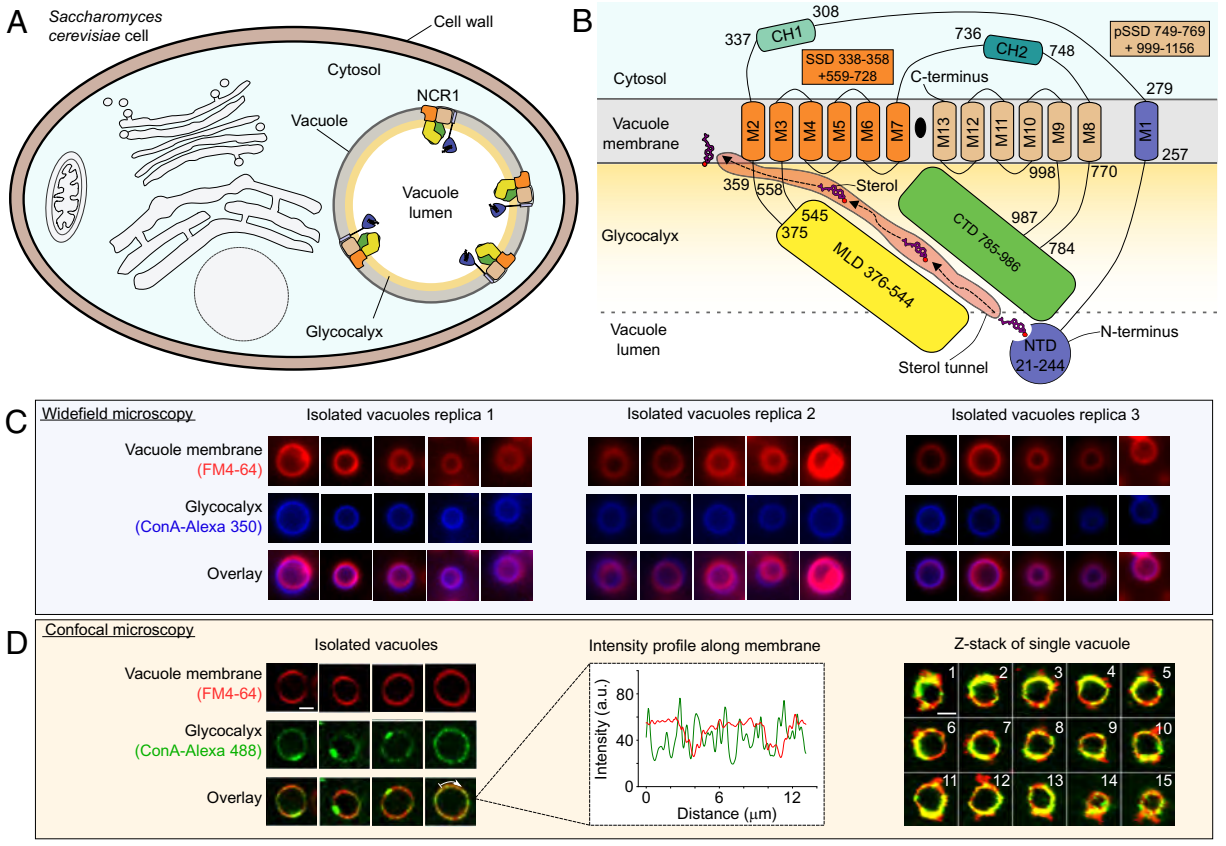

Fig. 1. Presence of a glycocalyx in yeast vacuoles. (*A*) *S. cerevisiae* cell organization highlighting the location of NCR1 in the acidic vacuole. (*B*) Topology of NCR1. Sterol molecules are shown moving from the NTD through the tunnel and into the vacuolar membrane. (*C*) Isolated vacuoles from three replicates imaged by widefield microscopy. Vacuolar membranes were stained red with lipophilic dye FM4-64, and the glycocalyx was stained blue with Concanavalin A conjugated to Alexa Fluor 350 (ConA-Alexa 350). (*D*) Isolated vacuoles imaged by confocal microscopy. Vacuolar membranes were stained red with lipophilic dye FM4-64, and the glycocalyx was stained green with Concanavalin A conjugated to Alexa Fluor 488 (ConA-Alexa 488). Intensity profile along the circumference of the indicated vacuolar membrane is shown together with slices from a Z-stack of an isolated vacuole, acquired every 0.25 μm.

implicated more broadly in coupling of a variety of RND family members to electrochemical membrane potential (15–22). A similar network is found in NPC proteins centered on a conserved acidic pair, Asp631 and Glu1068 in NCR1, which have been shown to be essential for the function of both NCR1 and NPC1 (7, 12, 23). In analogy to AcrB, it has been proposed that protons might provide the driving force for sterol movement through NPC by harnessing the pH gradient across lysosomal and vacuolar membranes (1). Structures of human NPC1 at pH 5.5 and pH 8.0 have indeed revealed distinct, pH-dependent conformations, but these structural changes were ascribed to a hypothetical autoinhibitory mechanism which was proposed to suppress activity prior to arriving in the lysosome/vacuole (12). A mechanistic model for sterol transport through the tunnel, as well as energy requirements, including possible coupling to the transmembrane proton gradient, remain unclear. It is also unclear whether NTD loading and transfer in the NPC proteins are rigidly coupled to their transport cycle or whether the NTD functions independently of the RND core domains (SSD + MLD and pSSD + CTD) (1).

Here, we provide evidence that the glycocalyx is present in yeast vacuoles, confirming a defining role of NCR1 as a way for sterols to cross the glycocalyx and reach the vacuolar membrane. To further explore the action of protons in this process, we solved cryo-EM structures of NCR1 at pH 5.5 and pH 7.5. These structures show that the NTD of NCR1 is not involved in the sterol transport mechanism, but that it serves instead as a tethered binding domain to receive substrate and transfer it to the tunnel. Additionally, the structures reveal distinct conformational changes that are consistent with two key states of a cycle driven by protonation and deprotonation of the acidic pair. In particular, a series of residues link the acidic pair to the SSD gate and coordinate interdomain movements between the MLD and the CTD, driving sterol movement through the tunnel toward the membrane.

Results

Staining Supports a Glycocalyx in the Yeast Vacuole. To establish the presence of a glycocalyx at the vacuolar membrane, we isolated vacuoles from *S. cerevisiae* and stained them with FM4-64, a lipophilic dye used for visualizing vacuole morphology. Concanavalin A, a lectin that selectively binds α-mannopyranosyl and α-glucopyranosyl glycoproteins, was used to probe for the glycocalyx. Widefield microscopy (Fig. 1*C*) shows vesicles in the expected size range for vacuoles (2 to 5 μm), many of which displayed colocalization of lipid and saccharide staining, consistent with the presence of a glycocalyx. To confirm this result and potentially assess the sidedness of the glycocalyx, higher-resolution confocal laser scanning microscopy was employed. Although colocalization was confirmed, the resolution was insufficient to determine the sidedness of the saccharide signal (Fig. 1*D*). Quantification of the intensity profile revealed a patchy distribution for both lipid and saccharide stain, with the saccharide stain showing higher variation, both in single images and Z-stacks (Fig. 1*D*).

Overall, the staining efficiency for saccharides ranged from 25 to 50% (*SI Appendix*, Fig. S1*A* and *B*). The relatively low efficiency could be due to impurities from other vesicles of the endomembrane

system, or difficulty of stain penetrating the vacuolar membrane. It is possible that saccharide staining occurs only if vacuoles are transiently opened or flipped inside/out during the isolation procedure. Nonetheless, these results support the presence of a glycocalyx in yeast vacuoles.

Structures of NCR1 Show Two Key Conformations. To assess the role of protons in sterol transport, we examined whether NCR1 adopted different conformations at high and low concentrations of protons. Specifically, we utilized pH 5.5 (high proton concentration) and pH 7.5 (low proton concentration) to mimic high and low protonation states of NCR1, respectively, and solved structures under these conditions (Fig. 2 *A* and *B* and *SI Appendix*, Figs. S2–S6 and Table S1).

We solved the structure of NCR1 at pH 7.5 using glyco-diosgenin (GDN) as the detergent at a resolution of 3.3 Å (Figs. 2*A* and 3 *A* and *B* and *SI Appendix*, Fig. S2). In this structure, an ergosterol is present in the NTD and two cholesterol hemisuccinate (CHS) molecules are found: one in the tunnel between the MLD and CTD and one at a hydrophobic patch between M1 and the pSSD (Figs. 2*A* and 3 *A* and *B* and *SI Appendix*, Fig. S7). The presence of CHS likely reflects the addition of this amphiphile during initial solubilization of cell membranes, whereas ergosterol was likely bound in vivo and copurified with NCR1. Notably, the conformation revealed by this structure is similar to that observed in the previously published crystal structure of NCR1 (PDB code 6R4L) (7).

We then proceeded to solve the structure at pH 5.5 in GDN, also at a resolution of 3.3 Å (Figs. 2*B* and 3 *C* and *D* and *SI Appendix*, Fig. S3). In this second structure, a GDN detergent molecule was found in addition to one ergosterol and two CHS molecules (Figs. 2*B* and 3 *C* and *D* and *SI Appendix*, Fig. S7). The GDN molecule is located at the bottom of the tunnel near the NTD. One CHS is located in the tunnel near the membrane surface—displaced compared to the first structure—while the other

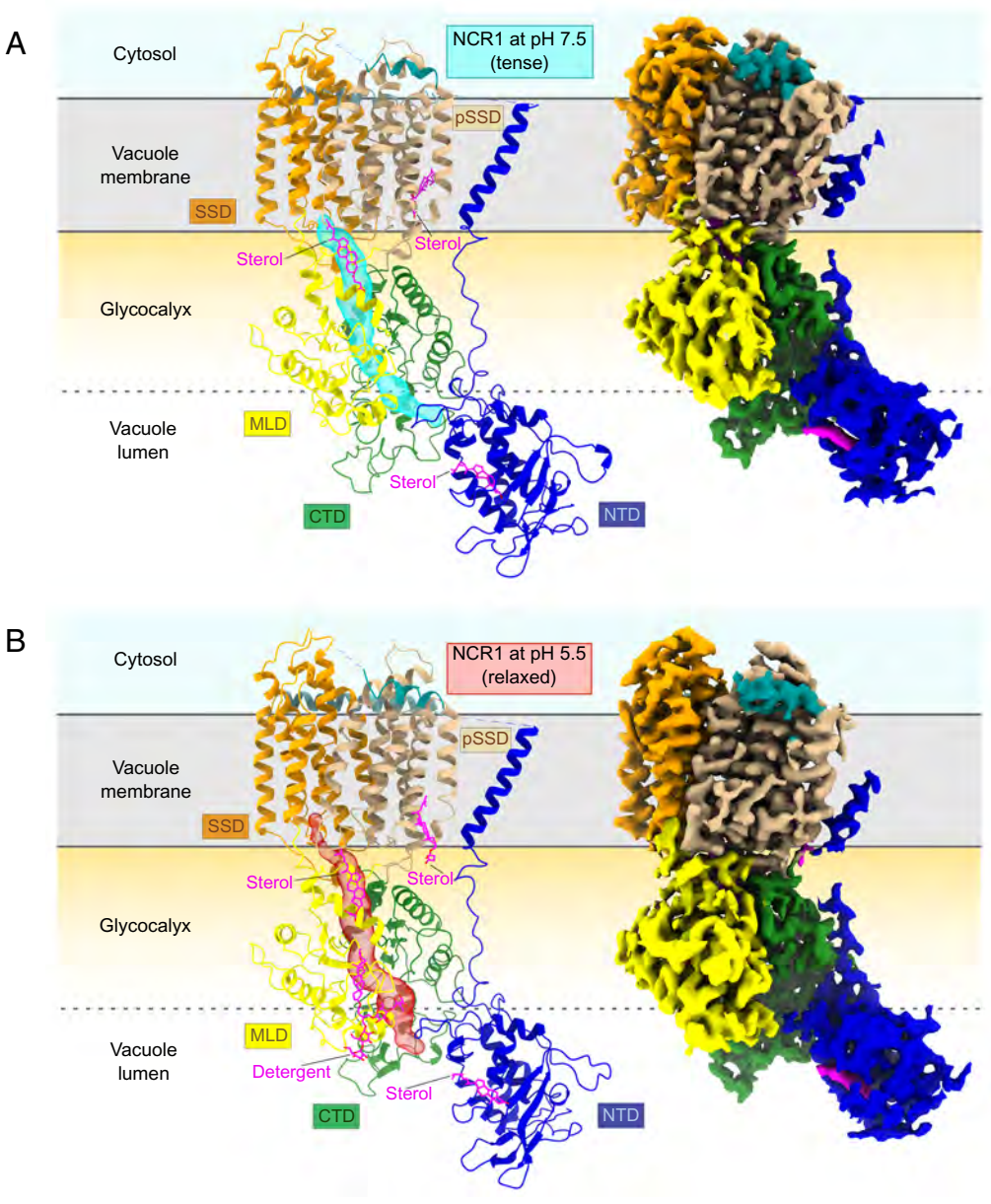

Fig. 2. Comparison of NCR1 structures at pH 7.5 and pH 5.5. (*A*) Model and map of NCR1 in GDN detergent at pH 7.5. A tunnel (cyan) stretches from the NTD to the SSD. Ligands are depicted in magenta and include an ergosterol in the NTD, a CHS in the tunnel, and a CHS in a hydrophobic patch between the pSSD and M1. (*B*) Model and map of NCR1 in GDN detergent at pH 5.5. The tunnel (red) and the three sterol ligands are accompanied by a GDN detergent molecule in the lower part of the tunnel.

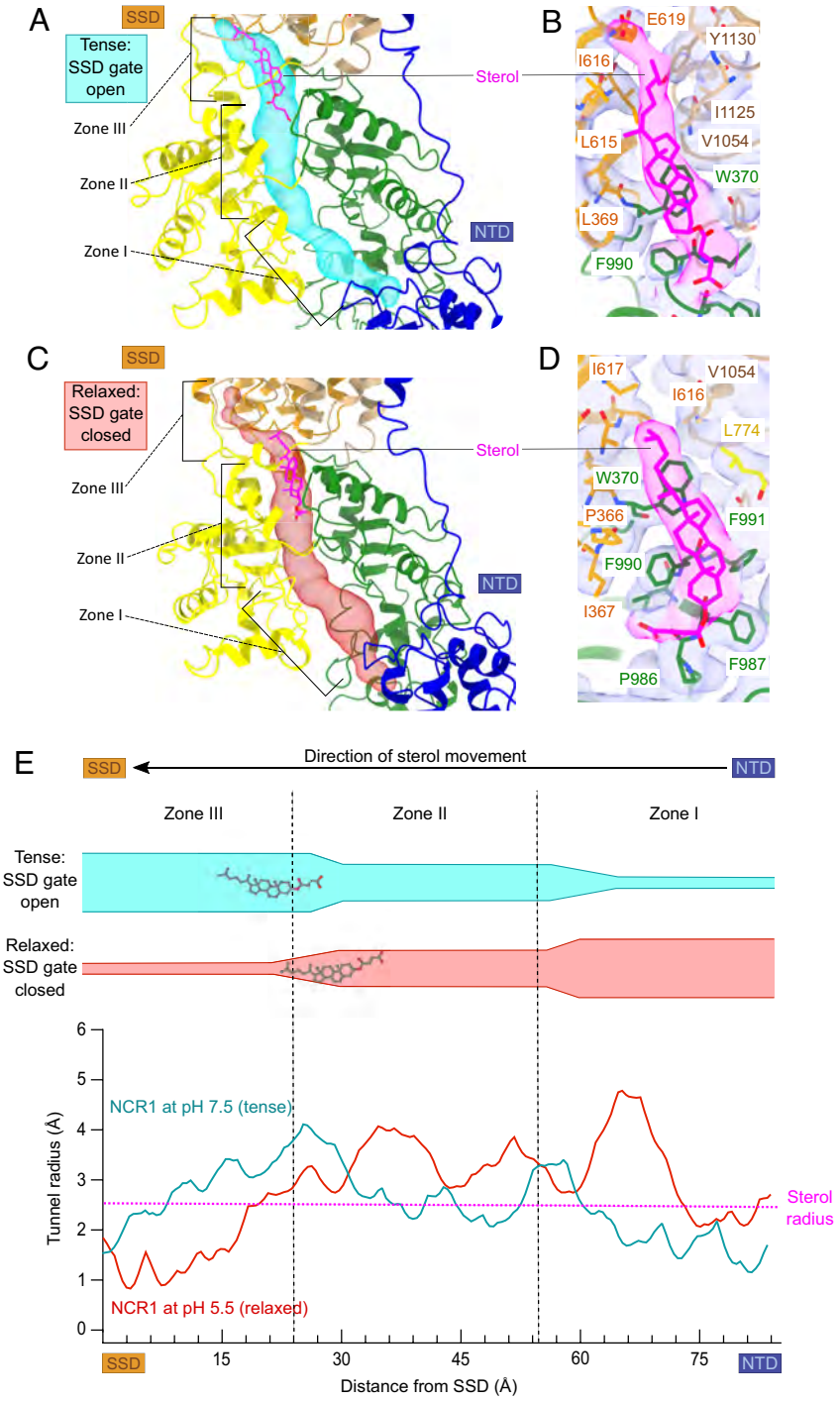

Fig. 3. Comparison of NCR1 tunnel profiles at pH 7.5 and pH 5.5. (*A*) Detail of the NCR1 model at pH 7.5 with the tunnel (cyan) formed between the MLD (yellow) and the CTD (green). Tunnel surface rendered by CAVER with zones I, II, and III indicated. (*B*) Map densities and model of NCR1 in GDN at pH 7.5 showing CHS molecule in magenta. (*C*) NCR1 model at pH 5.5 with tunnel surface (red) rendered by CAVER with zones I, II, and III indicated. (*D*) Map densities and model of NCR1 in GDN at pH 5.5 showing CHS molecule in magenta. (*E*) Graph of the tunnel radius vs. distance from the SSD for NCR1 at pH 7.5 (cyan) and pH 5.5 (red). Zones I, II, and III are delineated by black dotted vertical lines with a schematic representation of the tunnels that indicate the sterol location above the graph. The magenta dotted horizontal line corresponds to the sterol radius of 2.5 Å.

CHS molecule occupies the same hydrophobic patch between M1 and the pSSD. The ergosterol occupies its previously observed position in the NTD (Fig. 3*C* and *SI Appendix*, Fig. S7).

Comparison of the two structures at pH 7.5 and pH 5.5 reveals a series of key differences, making it clear that the structure at pH 5.5 adopts a different conformation compared to the structure at pH 7.5. When considered individually, RMSD of Cα atoms ($RMSD_{C\alpha}$) comparing MLD, CTD, SSD, and pSSD are minimal: 0.6 Å for CTD and 0.9 Å for MLD, 1.2 Å for SSD and 1.0 Å for pSSD. However, rigid body movements between the domains are apparent in the context of the entire molecule. In the transmembrane region, superposition of the SSD reveals a ~2.5 Å rigid-body displacement of the pSSD. That is, in the structure at pH 5.5, the SSD and pSSD are farther apart and adopt a distinct conformation between the two transmembrane domains we name the "relaxed" conformation. In contrast, the SSD and pSSD are closer together

at pH 7.5, which we name the "tense" conformation (*SI Appendix*, Fig. S8*A* and Table 1). There is also a movement of the CTD relative to the MLD: after structural alignment of the CTD, there is a ~3 Å displacement and slight rotation of the MLD in the two conformations (*SI Appendix*, Fig. S8*B*). Rotamers and interactions of side chains at the tunnel interface remain unchanged as a result of this conformational change, supporting a purely rigid body rotation between the MLD and CTD.

Because GDN occupied the tunnel at pH 5.5, we solved an additional structure in lauryl maltose neopentyl glycol (LMNG) detergent to rule out any influence of GDN on the observed conformation (*SI Appendix*, Figs. S4 and S9*A*). This third structure, also at pH 5.5 at 3.3 Å resolution, is devoid of GDN or other detergent molecules that could influence the conformation, but still retains the sterols found in the other two structures (*SI Appendix*, Fig. S7). It is in the relaxed conformation and essentially identical to the structure in GDN at pH 5.5 ($RMSD_{C\alpha}$ of 0.8 Å) with the acidic pair in the same position (*SI Appendix*, Fig. S9*B*), indicating that the GDN detergent molecule is not the determinant of the relaxed conformation.

In all the structures, the ligand positions are well defined. However, both here and in previous work on NCR1 and human NPC1, the poses adopted by ligands in the tunnel have been ambiguous due to limited resolution. An amphipathic helix solubilization system, called peptidisc, has been shown to lock proteins in defined conformations, often improving resolution (24, 25). Indeed, use of peptidisc improved the resolution of NCR1 to 2.4 Å (*SI Appendix*, Figs. S5 and S10*A*), thus enabling us to confirm the pose of sterol within the tunnel, with the hydroxyl group oriented toward the luminal tunnel entrance (*SI Appendix*, Fig. S10*B*) as modeled in the X-ray structure and as suggested by earlier work (26). In addition, water molecules are visible in a cavity within the membrane domain near the acidic pair (*SI Appendix*, Fig. S10*C*). However, this peptidisc structure adopts the relaxed conformation seen at pH 5.5, even though it was produced at pH 7.5 and the NTD and M1 helix were not visible at any stage during image processing. In parallel, we solved an additional structure at pH 7.5 in LMNG to 3.3 Å with features similar to the peptidisc sample: no density for the NTD or M1, and a relaxed conformation of the SSD and pSSD ($RMSD_{C\alpha}$ of 0.9 Å relative to peptidisc structure). This suggests that the lipid and detergent environment influence the ability of the M1 helix and the NTD to associate with the RND core and potentially also restrict movements of the RND core domains. Innate flexibility of the NTD and M1 helix is consistent with the lower resolution of these elements compared to the RND core in all our structures, indicating loose association with the core. In fact, in all the protein–detergent datasets, we identified a subpopulation of particles that produced structures lacking the NTD and M1 helix (*SI Appendix*, Figs. S2*E*, S3*E*, and S4*E*). However, the RND core displayed negligible differences when structures from the subpopulations (with and without NTD) were compared ($RMSD_{C\alpha}$ 0.10 Å for NCR1 at pH 5.5 and 0.04 Å for NCR1 at pH 7.5). The flexibility of the NTD has been suggested to assist in loading of the sterol. It is therefore noteworthy that, in the current maps, stabilization of the NTD had no effect on the RND core domains.

Changes in the Tunnel Shape Drive Sterol Transport. The dimensions of the tunnel, formed by the MLD and CTD, undergo substantial changes because of the conformational shifts between these two domains. Tunnel radius profiles of the two GDN structures were calculated from the NTD to the beginning of the SSD gate (Fig. 3 *A* and *C*), thus revealing three distinct zones: zone I near the NTD, zone II in the middle of the MLD and CTD, and zone III near the SSD gate. In the relaxed conformation, zone I is broad with the radius peaking at 4.8 Å, while the same zone narrows to average radius around 2 Å in the tense conformation (Fig. 3*E*). Zone III displays the inverse behavior, with the tunnel narrowing considerably to an average radius of 2 Å in the relaxed conformation, whereas the tunnel expands to ~3 Å radius in the tense conformation. In zone II, the differences between the two conformations are minimal with an average radius of ~3 Å. A broader comparison of NCR1 structures indicates that tunnel profiles strongly correlate with the conformation of the transmembrane domain: the tunnel profile for NCR1 at pH 7.5 is consistent with that from the X-ray structure, and both are in the tense conformation, whereas structures in the relaxed conformation have the opposite tunnel radius profile (*SI Appendix*, Fig. S11). This correlation indicates allosteric coupling between the membrane domain (tense vs. relaxed) and the MLD and CLD, which determine the tunnel shape. Furthermore, these comparisons suggest that concerted expansion and contraction of the tunnel is linked to the tense and relaxed conformation of the transmembrane domain and potentially represents a mechanism for propelling the sterol through the tunnel. This mechanism is consistent with changes in the position of the sterol observed within the tunnel. Specifically, there is well-defined density for sterol at the boundary of zones II and III (Fig. 3 *C* and *D*) in the relaxed conformation, whereas in the tense conformation the corresponding density is noticeably elongated and displaced ~6 Å toward the SSD gate (Fig. 3 *A* and *B*). This observation illustrates mobility of the sterol within the tunnel, which increases as it gets closer to the tunnel exit.

The Acidic Pair Network Links Tense and Relaxed Conformations to Sterol Transport. A network of interactions at the pseudosymmetry axis, relating the SSD to the pSSD, govern transition between the tense and relaxed conformations. This network centers on the conserved acidic pair, Asp631 (M5) and Glu1068 (M11), which alternately interact with His1072 (M11) and Lys1111 (M12) (Fig. 4*A* and *SI Appendix*, Fig. S6). In particular, the acidic pair coordinate His1072 (distance < 3.5 Å) in the tense conformation (NCR1 at pH 7.5), characterized by tight packing between SSD and pSSD. In the relaxed conformation (NCR1 at pH 5.5), the acidic pair pivots downward to form a new interaction with Lys1111 (also < 3.5 Å, Fig. 4*B*). Lys1111 undergoes the most dramatic movement,

Table 1. Summary of the conformations of NCR1 solved by X-ray crystallography and cryo-EM

Conformation	Tense		Relaxed		
SSD gate	Open		Closed		
Acidic pair network	D631-E1068-H1072		D631-E1068-K1111		
Sterol location	Zone III	Zone I	Zone II	Zone II	Zone II
Condition	pH 7.5 GDN	pH 6.1 LCP	pH 5.5 GDN	pH 5.5 LMNG	pH 7.5 Peptidisc
PDB	8QEB	6R4L	8QEC	8QED	8QEE

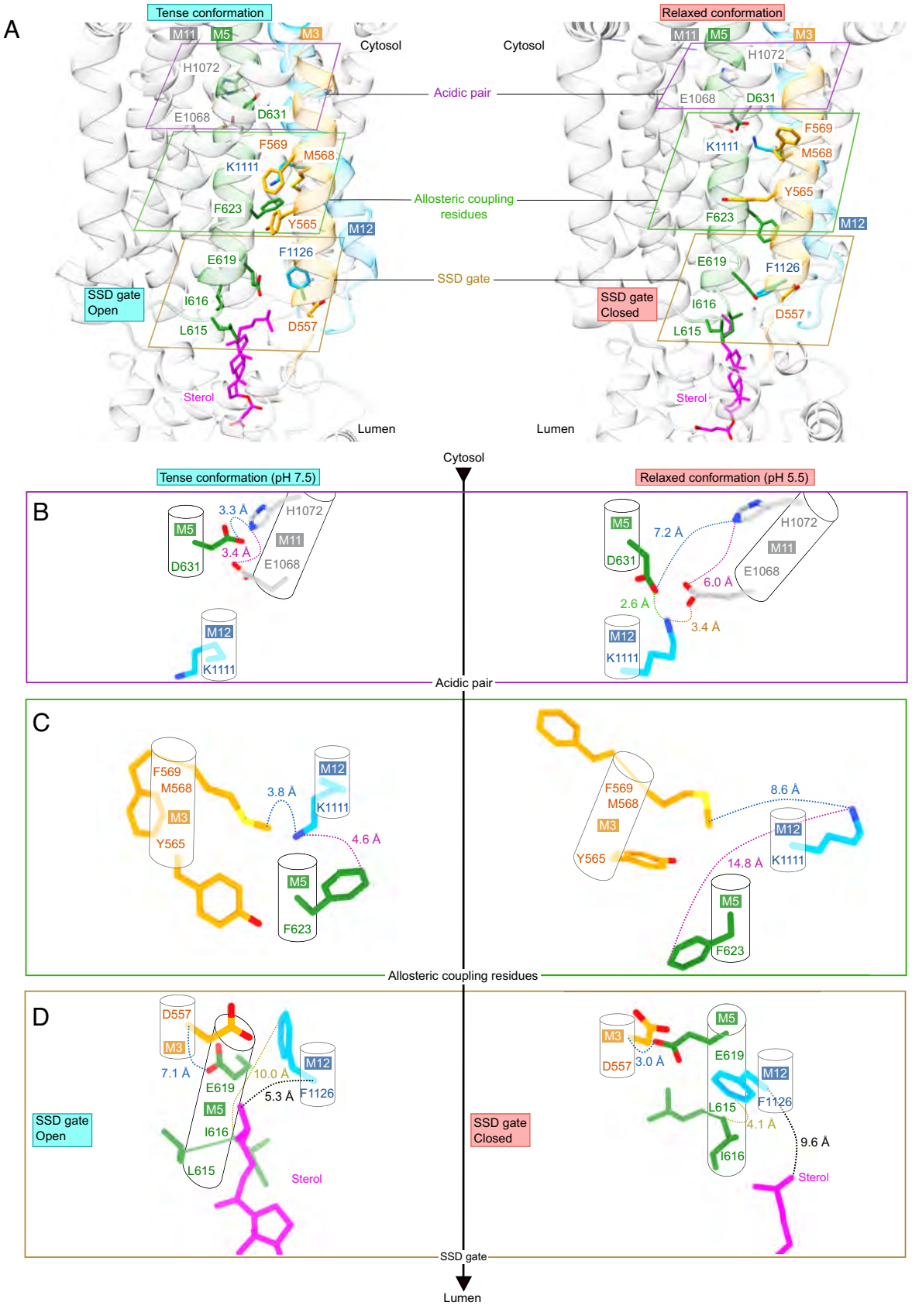

Fig. 4. Acidic pair and allosteric coupling residues controlling the opening and closing of the SSD gate. (*A*) Transmembrane domains of tense (*Left*) and relaxed (*Right*) conformations viewed parallel to the membrane. Key residues are shown on M3 (orange), M5 (green), M11 (gray), and M12 (blue). Sections parallel to the membrane are shown in subsequent panels to illustrate the acidic pair (purple box), allosteric coupling residues (green box), and the SSD gate (yellow box). (*B*) The acidic pair and interacting residues in the tense (*Left*) and relaxed (*Right*) conformations. (*C*) Allosteric coupling residues from M3, M5, and M12 in the tense (*Left*) and relaxed (*Right*) conformations. (*D*) Residues at the SSD gate controlling release of sterol (magenta) in the tense (*Left*) and relaxed (*Right*) conformations.

being buried between M3 and M5 in the tense conformation, and swinging toward the acidic pair in the relaxed conformation, thus drawing them away from His1072 (Fig. 4*C*).

Although density for acidic side chains is often weak or absent in cryo-EM maps (27), movement of Glu1068 toward Lys1111 in the relaxed conformation is clearly supported at a lower density threshold (*SI Appendix*, Fig. S6). In the case of Asp631, the specific side chain orientation remains ambiguous in the relaxed conformation despite attempts at focused alignment and density modification. Nevertheless, it is clear that the position of the SSD relative to the pSSD in the relaxed conformation prevents the interaction of the two acidic residues with His1072. Instead, swinging of Lys1111 toward the acidic residues induces a change in rotamers to promote an alternative interaction network. As a result, this new interaction drives displacement of the SSD relative to the pSSD and causes the two transmembrane domains to adopt the relaxed conformation (Fig. 4*B* and *SI Appendix*, Fig. S6). The looser association of these domains is also evidenced by the small cavity seen in the relaxed conformation, which is occupied by several water molecules that are visible in the higher-resolution peptidisc structure (*SI Appendix*, Fig. S10*C*).

The transition between these two states is allosterically coupled to the SSD gate and the conformation of the tunnel, thus controlling integration of sterol into the membrane. M5 undergoes displacement during this transition, making it a plausible element for allosterically linking the acidic pair to the opening or closing of the SSD gate (Fig. 4*C*). Specifically, the SSD gate is governed by movements at the luminal ends of M3, M5, M12, and their associated loops. The luminal side of M3 becomes more mobile when the gate is open, leading to weaker map density (*SI Appendix*, Fig. S6). In the transition from relaxed to tense conformation, the distance between Glu619 (M5) and Asp557 (M3) increases from 3.0 Å to 7.1 Å and the distance between Ile616 and Phe1126 increases from 4.1 Å to 10 Å (Fig. 4*D*). These changes are due to a swing of the Phe1126 sidechain as well as reconfiguration of the M4/M5 loop and the first turn of M5; together, they serve to control passage of sterol through the SSD gate. This opening and closing of the SSD gate is correlated with widening and narrowing of zone III of the tunnel, promoting sterol transport. Indeed, our structures show that as the gate opens in the tense conformation, the sterol molecule in the tunnel moves ~6 Å toward the membrane with its aliphatic tail protruding through the gate and ready for integration into the membrane (Fig. 4*D*).

Discussion

In lysosomes, low pH combines with hydrolytic enzymes to break down metabolites for recycling. In yeast and plants, the vacuole fulfills this function in addition to its role in storage of nutrients and ions (1, 7, 28, 29). For the lysosome, it is well established that the inner leaflet of the membrane is protected against autodigestion by the glycocalyx (30, 31). It is therefore reasonable to expect a similar barrier for the inner membrane of vacuoles. Here, we demonstrate colocalization of lipid and saccharide stain, thus supporting the presence of a glycocalyx in yeast vacuoles as a shared feature of degradative organelles.

An unresolved question regarding the function of NPC proteins is whether loading and transport of sterol are coupled or whether loading of the NTD is independent of the ensuing transport through the tunnel (1). Our data suggest the latter: that the NTD acts as a tethered binding domain with no discernible allosteric coupling to the transport process. Specifically, comparison of structures with and without the NTD shows that NTD association to the RND core has no observable effect on the conformations of MLD and CTD ($RMSD_{C\alpha}$ of ≤0.1 Å). Since the resolution was lower in the structures without the NTD, we could not confidently position side chain rotamers to calculate tunnel profiles, but assuming identical rotamers (as observed for tense and relaxed conformations), the tunnel profiles would also be the same. In all our structures, the NTD is loaded with ergosterol and oriented in a postloading state, despite pH-dependent conformational changes to the RND core. Indeed, analysis of *npc* genes in eukaryotes has previously shown that some fungal genomes encode the NTD as a separate gene product that is not covalently linked to the RND core, reinforcing the importance of the NTD for sterol delivery, but not necessitating it to be part of a single polypeptide chain (32). Earlier studies of the human sterol transporter, NPC1, without the NTD support this idea by showing that a nontethered NTD can still transfer substrate to the core domains (33). Nevertheless, tethering of the NTD to the RND core could serve to increase local sterol concentration and thereby increase the efficiency and specificity of the transfer process (34). It is also noteworthy that the association of the NTD and M1 and the movements of the SSD and pSSD appears highly dependent on the lipid/detergent environment. For future work, it would be relevant to replace detergents with, e.g., a lipid/nanodisc system to better mimic the physiological lipid bilayer environment.

The high resolution of the NCR1 structure solved in peptidisc offers valuable insights into the orientation of sterol and clearly shows that the polar head group of the sterol faces toward the luminal entrance to the tunnel (*SI Appendix*, Fig. S10*B*). This pose supports the hand-off model for the NTD loading step, which positions the sterol to be transferred into the tunnel in the optimal orientation for integration into the inner leaflet of the organellar membrane (26).

Our analysis of the two different conformations of NCR1 indicates that the tunnel changes its profile due to rigid body movement of the MLD relative to the CTD (Fig. 3 *A* and *C* and *SI Appendix*, Fig. S8*B*). Similar conformational changes have been observed in other RND proteins and they are proposed to generate a peristaltic mode of transport in the multidrug efflux transporter AcrB (15, 35). Indeed, these changes are accompanied by a shift in the sterol position within the tunnel of NCR1. In this respect, it is notable that transport was abolished when cysteine cross-linking was used to prevent interdomain movements of MLD and CTD in NPC1 (36).

For human NPC1, pH-dependent conformational changes have been ascribed to an inhibitory mechanism: The high pH form was postulated to represent an inactive state, adopted while the protein is trafficked through the endomembrane system, while the low pH form was described as a constitutively active state achieved within the lysosome (12). However, the configuration of the SSD gate in the two NPC1 structures and now in our NCR1 structures is in conflict with this mechanism: the SSD gate is open at high pH, when the protein should be inactive, and closed at low pH, when the protein should have been active. Alternatively, the energy coupling mechanism employed by AcrB and other RND superfamily members, together with our observations of sterol displacement in the tunnel of our structures, suggest a different interpretation of the pH-dependent conformational change.

Here, we propose an alternative model to explain the mechanism of NPC proteins, where the tense and relaxed conformations represent two key conformations in a proton-driven sterol transport cycle (Fig. 5). In our model, the acidic pair Asp631 and Glu1068 in NCR1 forms a network analogous to AcrB at the interface of the SSD and pSSD (*SI Appendix*, Fig. S12) (15). Depending on the protonation state of the network—in our case induced by pH of the sample—interactions are made with either

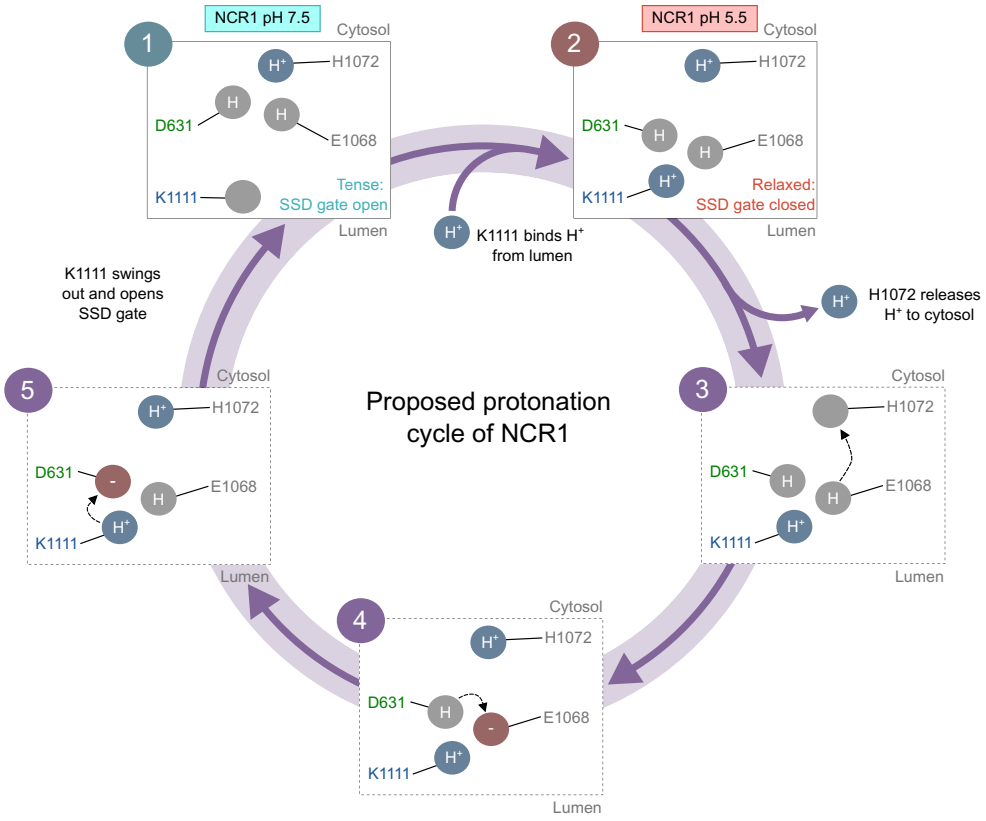

Fig. 5. Proposed protonation cycle driving sterol transport by NCR1. The protonation cycle involves five steps: (1) Asp631 and Glu1068 interact with His1072 in the tense conformation, where the SSD gate is open (NCR1 pH 7.5). (2) Lys1111 binds a proton from the lumen, causing it to move toward and interact with Asp631 and Glu1068, thus producing the relaxed conformation where the SSD gate is closed (NCR1 pH 5.5). (3) His1072 releases its proton to the cytosol and is then reprotonated by E1068. (4) D631 reprotonates E1068. (5) Lys1111 reprotonates Asp631 and then swings away from Asp631 and E1068. The protonation state of the residues is reestablished for the next protonation cycle to occur. Colors correspond to positively charged (blue), neutral (gray), and negatively charged (red) residues.

His1072 or Lys1111. Thus, our model invokes a cycle with Lys1111 being the initial proton acceptor from the lumen in the tense conformation (Fig. 5, step 1). When Lys1111 accepts a proton, perhaps via Glu619 and Tyr565, it swings toward the acidic pair, inducing the relaxed conformation. As a result, the SSD gate closes and there is a coordinated narrowing of zone III and widening of zone I of the tunnel (Fig. 5, step 2). Formation of the tripartite network between the acidic pair and Lys1111 induces His1072 to release a proton to the cytosol (Fig. 5, step 3). Asp631 and Glu1068 now engage in a 3-step transfer of the proton from Lys1111 to His1072 (Fig. 5, steps 3–5). After donating its proton, Lys1111 swings back into the initial position, nestled into a hydrophobic pocket between M3 and M5, while the acidic pair changes conformation to interact with His1072 to generate the tense conformation. Together, these changes lead to a conformational shift of the MLD and CTD, driving peristaltic movements of sterol within the tunnel and opening the SSD gate (Fig. 5, step 1). Binding of another luminal proton to Lys1111 initiates the next cycle of peristaltic movement.

Our proposed model is consistent with a generalized model for the function of proteins in the RND superfamily. The transmembrane domain—specifically the symmetry point between the SSD and pSSD—functions as a motor driven by proton binding (or monovalent cation binding for some RND proteins), which cycles the SSD and pSSD between relaxed and tense conformations. This cycle leads to movements of the effector or luminal domains, which in NPC proteins cause the MLD and the CTD to concertedly either contract or expand zone I and zone III of the tunnel to propel sterol toward the membrane. A similar alternation between a tense and relaxed conformation of the transmembrane domain in the protein Dispatched, another RND protein, is suggested to be central for its function in Sonic Hedgehog mobilization (21). Also noteworthy, a "breathing" motion, similar to the switch between relaxed and tense conformations we describe here for NCR1, has been shown for the transmembrane domains of the RND protein Patched and is suggested to provide energy for cholesterol egress through a similar tunnel (37). Finally, blocking the tunnels of either NPC1 or Patched has been demonstrated to prevent proper function (11, 12, 22, 38, 39). Collectively, these findings reported for other RND proteins support the model we propose here.

Although our model is consistent with our structural data and with functional studies of related members in the RND superfamily (e.g., refs. 7, 11, 12, and 35), it remains speculative in the absence of direct experimental validation. For NPC proteins, key residues have already been shown to be essential for function (7, 12), but further biochemical experiments, in the presence of a glycocalyx, where the role of protons is explicitly addressed are necessary. Also, mutational analyses in a cellular context will need to consider broader impacts on the homeostasis of organelles and sterol metabolism which may be secondary to specific effects on the transport mechanism.

In conclusion, we have presented evidence for a glycocalyx in the *S. cerevisiae* vacuole and have provided a detailed structural analysis of NCR1 in two distinct conformational states. We have linked changes in tunnel dimensions and sterol molecule locations to changes of the acidic pair in the transmembrane region. Our model suggests that the conformational transition is dependent on

the protonation state of titratable residues in the transmembrane domains, implying that sterol transport is linked to the proton motive force found across the vacuolar/lysosomal membrane. Our model contrasts with the previously proposed model where the two observed conformations represent an active and inactive form. More direct biochemical data will be needed to discriminate definitively between these alternative scenarios. Nevertheless, our model is consistent with a general scheme for transport in the RND superfamily and offers insights into how NPC proteins adapt a generalized RND mechanism to move sterols past the glycocalyx and into the lysosomal/vacuolar membrane.

Materials and Methods

Glycocalyx Staining and Visualization. Vacuoles were isolated following the protocol outlined previously (40). Briefly, BY4741 cells (http://www.euroscarf.de/plasmid_details.php?accno=Y00000) were cultivated in standard Yeast Extract–Peptone–Dextrose (YPD) liquid media at 30 °C, 150 rpm to 0.8 to 1 at OD_{600}. Cells were harvested by centrifugation at 4,000×*g* for 5 min at room temperature and resuspended in 100 mM PIPES/KOH pH 9.4 and 10 mM DDM. After incubation at 30 °C for 10 min, cells were centrifuged as before, and the pellet was gently resuspended in 50 mM potassium phosphate pH 7.5, 0.6 M sorbitol, and 0.16× YPD, supplemented with 2 mg/mL Zymolyase. The resulting spheroplasts were incubated at 30 °C for 25 min and then centrifuged at 4 °C for 5 min at 2,500×*g*. Subsequently, the pellet was resuspended in 15% Ficoll, 10 mM PIPES/KOH pH 6.8, and 200 mM sorbitol and incubated on ice for 2 min, followed by 75 s at 30 °C. The resulting cell lysate was transferred to ultracentrifuge tubes and layered with a discontinuous Ficoll (Sigma) gradient consisting of 8, 4, and 0%. After centrifugation at 110,000×*g* for 90 min at 4 °C, vacuoles were collected from the interface between the 4% and 0% layers of Ficoll. These vacuoles were stained with FM4-64 (Thermo Scientific) at a final concentration 2.5 μg/mL for 1 h at 4 °C followed by Concanavalin A conjugated with Alexa Fluor 350 (Thermo Scientific) at a final concentration of 0.5 mg/mL for 3 h at 4 °C. Visualization of both stains was conducted with a Zeiss Axio Observer Z1 widefield microscope equipped with a 63× objective under oil immersion.

For confocal microscopy, vacuoles were stained with Concanavalin A conjugated with Alexa Fluor 488 (Thermo Scientific) at a final concentration of 100 μg/mL for either 30 min at room temperature or 3 h at 4 °C. Additionally, the vacuoles were stained with FM4-64 (Thermo Scientific) at a final concentration of 2 μg/mL for either 30 min at room temperature or 1 h at 4 °C. Confocal images were acquired by a Nikon A1 confocal microscope equipped with a 100× oil objective. Images were aligned by automated translation and rotation using plugins to ImageJ (41). Intensity line profiles of FM4-64 and ConA-Alexa 488 were measured using Macros in ImageJ and plotted in Python software using Matplotlib (42).

Homologous Expression of NCR1 and Membrane Preparation. Protein expression of codon-optimized NCR1 from *S. cerevisiae* (UniProt: Q12200) was performed as described previously (7). For expression, *S. cerevisiae* strain DSY-5 was transformed with an expression vector based on p423_GAL1 (43) carrying full-length *ncr1* with a C-terminal deca-histidine tag and grown to high density in a bioreactor and harvested after a 22 h induction using galactose (44). Cells were harvested by centrifugation at 2,500×*g* for 10 min at 4 °C and the pellets were stored at −70 °C.

Cells were homogenized with a beadbeater (Biospec Products) by mixing ~200 g of cells with 750 mL lysis buffer (600 mM NaCl, 100 mM Tris-HCl pH 7.5, and 1.2 mM PMSF) in prechilled metal canisters containing 0.5 mm glass beads (BioSpec Products) with five cycles of agitation (1 min on and 2 min off). The cell lysate was filtered and resupplied with 1.2 mM PMSF, and cell debris was removed by centrifugation at 17,000×*g* for 20 min at 4 °C. The supernatant was centrifuged at 200,000×*g* for 2 h at 4 °C, and the resulting membrane pellets were divided into 3 g aliquots and stored in 500 mM NaCl, 50 mM Tris-HCl, pH 7.5, and 20% (v/v) glycerol at −20 °C.

Purification of NCR1. Two aliquots of membranes (~6 g) were solubilized in basis buffer (500 mM NaCl, 50 mM Tris-HCl, pH 7.5, and 10% (v/v) glycerol, supplemented with 1% (w/v) cholesteryl hemisuccinate (CHS from Anatrace), 0.6% (v/v) *n*-dodecyl-β-D-maltoside (DDM from Inalco Pharmaceuticals), and 1.6 mg/mL iodoacetamide (Sigma-Aldrich) for 20 min at 4 °C. The sample was sonicated, filtered with 5 μm as well as 1.2 μm pore size syringe filters (Sartorius), and supplemented with 20 mM imidazole prior to loading onto a 5 mL HisTrap HP column (Cytiva) equilibrated with 20 mM imidazole and 0.017% DDM in basis buffer. The column was washed with 50 mL of basis buffer containing 70 mM imidazole and 0.017% DDM followed by 45 mL of G20 buffer (200 mM NaCl, 20 mM imidazole) supplemented either with 0.01 to 0.05% glyco-diosgenin (GDN from Antrance) or 0.025% LMNG, with pH of either 5.5 (20 mM MES) or 7.5 (20 mM Tris-HCl). Finally, 175 units of thrombin (Avantor) were added to cleave the His-tag, and 5 mL of this buffer was slowly circulated through the column at 4 °C overnight. The protein was eluted with 15 mL of the corresponding buffer containing 40 mM imidazole. After concentration, the sample was loaded onto a Superdex 200 10/300 GL Increase column (GE Healthcare), equilibrated with 200 mM NaCl, containing either 0.01 to 0.05% GDN at pH 5.5 (20 mM MES) or pH 7.5 (20 mM Tris-HCl) or 0.005% LMNG at pH 5.5 (20 mM MES). Peak fractions were pooled, concentrated to ~9 mg/mL, and immediately used to prepare EM grids.

Purification in peptidisc involved additional wash steps on the 5 mL HisTrap HP column (24, 25). After the 50 mL wash with 70 mM imidazole, the sample was further washed with 50 mL of 100 mM NaCl, 50 mM Tris-HCl pH 7.5, and 0,008% of DDM without imidazole followed by 45 mL of peptidisc buffer (100 mM NaCl, 50 mM Tris-HCl, pH 7.5, and 0.5 mg/mL peptidisc from GenScript). Of this buffer, 5 mL was circulated for 30 min at 4 °C followed by a final wash with 100 mM NaCl and 50 mM Tris-HCl pH 7.5. This solution was supplemented with thrombin and circulated overnight, as described earlier. Size-exclusion chromatography was performed using 100 mM NaCl and 10 mM Tris-HCl, pH 7.5, and the peak fraction of the monomer was concentrated to ~4 mg/mL.

Cryo-EM Sample Preparation, Imaging, and Image Processing. Samples were applied to glow discharged C-flat 1.2/1.3 μm Cu grids (Protochips, #M-CF313-100) and plunge-frozen in liquid ethane using a Vitrobot Mark IV (Thermo Scientific) at 4 °C and 100% humidity.

Images for NCR1 samples at pH 7.5 in GDN and peptidisc were collected at the Danish National cryo-EM facility, EMBION, at Aarhus University in Denmark at 130,000× magnification on a K3 detector (Gatan) with a raw pixel size of 0.647 Å and total dose of 60 $e^{-}/Å^2$. Images for NCR1 samples at pH 5.5 in GDN and LMNG were collected at the National Electron Bio-imaging Centre (eBIC), Oxford, United Kingdom 165,000× magnification on a K3 detector with a calibrated raw pixel size of 0.536 Å and a total dose of 60 $e^{-}/Å^2$. Defocus generally ranged from −0.6 to −2.5 μm for all four datasets.

Image processing workflows for each dataset are illustrated in *SI Appendix*, Figs. S2–S5. All processing steps were conducted in cryo-SPARC v3.3.1 (45). Briefly, the workflows involved patch-based motion correction, CTF estimation, curation to exclude poor quality images with CTF-estimated resolution >4 Å, high astigmatism, and thick ice. Templates were created from an initial set of particles and used for automated particle picking followed by two rounds of 2D classification using a 160 Å circular mask. The best classes were combined for multiple rounds of ab initio reconstruction with two classes to eliminate damaged particles, empty micelles, and other artifacts. The resulting structures were used as references for multiple rounds of heterorefinement, which typically separated particles with and without a visible NTD. Once a homogeneous set of particles was obtained, a final nonuniform refinement was performed to produce the final structure. Resolution was assessed using both the gold-standard FSC curve and a local resolution job.

Model Building and Refinement. A summary of the refinement statistics from all 4 models is shown in *SI Appendix*, Table S1. The crystal structure of NCR1 (PDB: 6R4L) was used as a template for model building. To start, this model was rigid-body fitted to each cryo-EM density map using Chimera (46) and then subjected to molecular dynamics flexible fitting (MDFF) (47) using Namdinator (48). For the peptidisc sample, the NTD and the M1 helix were removed. For NCR1 in LMNG at pH 5.5, the final model of NCR1 in GDN at pH 5.5 was initially docked into the map. Using these initial models, COOT v0.9.3 (49, 50) was used for manual adjustment of the polypeptide, addition of carbohydrates (NAG) at specific Asn residues (123, 401, 513, 900, and 940 depending on the model), and placement of ligands. These ligands included cholesteryl hemisuccinate (Y01), glyco-diosgenin (Q7G), phosphatidylethanolamine (PTY), and ergosterol (ERG)

(51). The models were gradually improved by iterative rounds of real-space refinement using PHENIX (52, 53) and manual adjustments in COOT. The final models were validated with MolProbity (54), CaBLAM (55), Ramachandran-Z analysis (Rama-Z) (56), and the PDB validation server (57).

Model Analysis and Figure Preparation. Caver Analyst 2.0 Beta (58) was used to identify and analyze the tunnels in NCR1 structures. Caver Analyst 2.0 Beta default parameters were used except that the shell radius was set to 9, the probe radius to 0.2, and the searches were initiated between Asp557 and Tyr1130. Structural figures were prepared with USCF Chimera v1.15 (46) and USCF ChimeraX v1.3 (59). SEC curves and sterol tunnel dimensions were plotted with GraphPad Prism v9 software (San Diego, CA). The multiple sequence alignment of RND protein members was made with PROMALS3D (60) and visualized in Aline (61). ImageJ (41) was used to view and adjust the contrast of micrographs from isolated vacuoles.

Data, Materials, and Software Availability. Atomic models have been deposited in the Protein Data Bank (PDB), and cryo-EM maps have been deposited in the Electron Microscopy Data Bank (EMDB). NCR1 in GDN at pH 7.5 (tense): PDB 8QEB and EMDB EMD-18350 (62); NCR1 in GDN at pH 5.5 (relaxed): PDB 8QEC and EMDB EMD-18351 (63); NCR1 in LMNG at pH 5.5: PDB 8QED and EMDB EMD-18352 (64); and NCR1 in peptidisc at pH 7.5: PDB 8QEE and EMDB EMD-18353 (65).

ACKNOWLEDGMENTS. We acknowledge The Danish National Cryo-EM Facility Aarhus Node at Aarhus University, where data were collected. We also thank Diamond Light Source's electron Bio-Imaging Centre for cryo-EM data collection. We acknowledge access to the computational infrastructure at the Center for Structural Biology at Aarhus University. We express our gratitude to the Bioimaging Core Facility at Aarhus University. Confocal image acquisition and deconvolution of the obtained images were performed at the Danish Molecular Biomedical Imaging Center. A.B. was supported by an Ukraine Research Fellowship from The Aarhus University Research Foundation and a "Scholars At Risk from Ukrainian Universities" fellowship. D.L.S. was supported by the NIH (Grant Agreement No. R35 GM144109). D.W. acknowledges funding from the Danish Research Council (grant ID: 2032-00139B). This work was supported by the Danish Council for Independent Research (Grant Agreement No. 0135-00032B), the Carlsberg Foundation (Grant Agreement No. CF19-0127), and the European Research Council (Grant Agreement No. 637372) to B.P.P.

Author affiliations: [a]Department of Molecular Biology and Genetics, Aarhus University, Aarhus C 8000, Denmark; [b]Department of Molecular Biology and Genetics, Aarhus Institute of Advanced Studies, Aarhus University, Aarhus C 8000, Denmark; [c]Department of Biochemistry and Molecular Biology, University of Southern Denmark, Odense M 5230, Denmark; and [d]Department of Biochemistry and Molecular Pharmacology, New York University School of Medicine, New York, NY 10016

1. M. B. L. Winkler *et al.*, Sterol uptake by the NPC system in eukaryotes: A *Saccharomyces cerevisiae* perspective. *FEBS Lett.* **596**, 160–179 (2022).
2. W. R. Evans, C. J. Hendriksz, Niemann–Pick type C disease–The tip of the iceberg? A review of neuropsychiatric presentation, diagnosis and treatment. *BJPsych. Bull* **41**, 109–114 (2017).
3. I. Ribeiro *et al.*, Niemann–Pick type C disease: NPC1 mutations associated with severe and mild cellular cholesterol trafficking alterations. *Hum. Genet.* **109**, 24–32 (2001).
4. A. C. Berger, P. K. Hanson, J. Wylie Nichols, A. H. Corbett, A yeast model system for functional analysis of the Niemann–Pick type C protein 1 homolog, Ncr1p. *Traffic* **6**, 907–917 (2005).
5. K. Malathi *et al.*, Mutagenesis of the putative sterol-sensing domain of yeast Niemann Pick C-related protein reveals a primordial role in subcellular sphingolipid distribution. *J. Cell Biol.* **164**, 547–556 (2004).
6. S. L. Sturley, Conservation of eukaryotic sterol homeostasis: New insights from studies in budding yeast. *Biochim. Biophys. Acta* **1529**, 155–163 (2000).
7. M. B. L. Winkler *et al.*, Structural insight into eukaryotic sterol transport through Niemann-pick type C proteins. *Cell* **179**, 485–497.e418 (2019).
8. L. Lehle, S. Strahl, W. Tanner, Protein glycosylation, conserved from yeast to man: A model organism helps elucidate congenital human diseases. *Angew. Chem. Int. Ed. Engl.* **45**, 6802–6818 (2006).
9. W. F. Neiss, A coat of glycoconjugates on the inner surface of the lysosomal membrane in the rat kidney. *Histochemistry* **80**, 603–608 (1984).
10. J. M. Tarbell, L. M. Cancel, The glycocalyx and its significance in human medicine. *J. Int. Med.* **280**, 97–113 (2016).
11. T. Long *et al.*, Structural basis for itraconazole-mediated NPC1 inhibition. *Nat. Commun.* **11**, 152 (2020).
12. H. Qian *et al.*, Structural basis of low-pH-dependent lysosomal cholesterol egress by NPC1 and NPC2. *Cell* **182**, 98–111.e118 (2020).
13. H. Nikaido, RND transporters in the living world. *Res. Microbiol.* **169**, 363–371 (2018).
14. P. A. Klenotic, M. A. Moseng, C. E. Morgan, E. W. Yu, Structural and functional diversity of resistance-nodulation-cell division transporters. *Chem. Rev.* **121**, 5378–5416 (2021).
15. M. Zwama, A. Yamaguchi, Molecular mechanisms of AcrB-mediated multidrug export. *Res. Microbiol.* **169**, 372–383 (2018).
16. O. Adams *et al.*, Cryo-EM structure and resistance landscape of M. tuberculosis MmpL3: An emergent therapeutic target. *Structure* 29, 1182–1191.e1184 (2021).
17. A. Furukawa, S. Nakayama, K. Yoshikaie, Y. Tanaka, T. Tsukazaki, Remote coupled drastic beta-barrel to beta-sheet transition of the protein translocation motor. *Structure* **26**, 485–489.e482 (2018).
18. M. A. Moseng *et al.*, Cryo-EM structures of CusA reveal a mechanism of metal-ion export. *Am. Soc. Microbiol.* **12**, e00452-21 (2021).
19. B. R. Myers, L. Neahring, Y. Zhang, K. J. Roberts, P. A. Beachy, Rapid, direct activity assays for smoothened reveal Hedgehog pathway regulation by membrane cholesterol and extracellular sodium. *Proc. Natl. Acad. Sci. U.S.A.* **114**, E11141–E11150 (2017).
20. H. K. Tam *et al.*, Allosteric drug transport mechanism of multidrug transporter AcrB. *Nat. Commun.* **12**, 3889 (2021).
21. Q. Wang *et al.*, Dispatched uses Na(+) flux to power release of lipid-modified Hedgehog. *Nature* **599**, 320–324 (2021).
22. Y. Zhang *et al.*, Structural basis for cholesterol transport-like activity of the hedgehog receptor patched. *Cell* **175**, 1352–1364 e1314 (2018).
23. X. C. Zhang, M. Liu, L. Han, Energy coupling mechanisms of AcrB-like RND transporters. *Biophys. Rep.* **3**, 73–84 (2017).
24. M. L. Carlson *et al.*, The Peptidisc, a simple method for stabilizing membrane proteins in detergent-free solution. *eLife* **7**, e34085 (2018).
25. K. L. Ung, H. Alsarraf, L. Kremer, M. Blaise, MmpL3, the trehalose monomycolate transporter, is stable in solution in several detergents and can be reconstituted into peptidiscs. *Protein Expr. Purif.* **191**, 106014 (2022).
26. H. J. Kwon *et al.*, Structure of N-terminal domain of NPC1 reveals distinct subdomains for binding and transfer of cholesterol. *Cell* **137**, 1213–1224 (2009).
27. M. A. Marques, M. D. Purdy, M. Yeager, CryoEM maps are full of potential. *Curr. Opin. Struct. Biol.* **58**, 214–223 (2019).
28. X. Tan *et al.*, A review of plant vacuoles: Formation, located proteins, and functions. *Plants (Basel)* **8**, 327 (2019).
29. A. Van Ho, D. M. Ward, J. Kaplan, Transition metal transport in yeast. *Annu. Rev. Microbiol.* **56**, 237–261 (2002).
30. M. Kosicek *et al.*, N-glycome of the lysosomal glycocalyx is altered in Niemann-pick type C disease (NPC) model cells. *Mol. Cell Proteom.* **17**, 631–642 (2018).
31. H. Q. Liu, J. Li, C. L. Xuan, H. C. Ma, A review on the physiological and pathophysiological role of endothelial glycocalyx. *J. Biochem. Mol. Toxicol.* **34**, e22571 (2020).
32. O. Adebali, A. O. Reznik, D. S. Ory, I. B. Zhulin, Establishing the precise evolutionary history of a gene improves prediction of disease-causing missense mutations. *Genet. Med.* **18**, 1029–1036 (2016).
33. M. N. Trinh, M. S. Brown, J. Seemann, J. L. Goldstein, F. Lu, Lysosomal cholesterol export reconstituted from fragments of Niemann-Pick C1. *eLife* **7**, e38564 (2018).
34. M. Dyla, N. S. Gonzalez Foutel, D. E. Otzen, M. Kjaergaard, The optimal docking strength for reversibly tethered kinases. *Proc. Natl. Acad. Sci. U.S.A.* **119**, e2203098119 (2022).
35. M. A. Seeger *et al.*, Structural asymmetry of AcrB trimer suggests a peristaltic pump mechanism. *Science* **313**, 1295–1298 (2006).
36. P. Saha *et al.*, Inter-domain dynamics drive cholesterol transport by NPC1 and NPC1L1 proteins. *eLife* **9**, e57089 (2020).
37. T. B. Ansell *et al.*, The energetics and ion coupling of cholesterol transport through Patched1. *Sci. Adv.* **9**, 15 (2023).
38. X. Qi, P. Schmiege, E. Coutavas, X. Li, Two patched molecules engage distinct sites on Hedgehog yielding a signaling-competent complex. *Science* **362**, eaas8843 (2018).
39. Y. Zhang *et al.*, Hedgehog pathway activation through nanobody-mediated conformational blockade of the Patched sterol conduit. *Proc. Natl. Acad. Sci. U.S.A.* **117**, 28838–28846 (2020).
40. S. E. Rieder, S. D. Emr, Isolation of subcellular fractions from the yeast *Saccharomyces cerevisiae*. *Curr. Protoc. Cell Biol.* **8**, 3.8.1–3.8.68 (2000).
41. J. Schindelin *et al.*, Fiji: An open-source platform for biological-image analysis. *Nat. Methods* **9**, 676–682 (2012).
42. J. D. Hunter, Matplotlib: A 2D graphics environment. *Comput. Sci. Eng.* **9**, 90–95 (2007).
43. D. Mumberg, R. Müller, M. Funk, Regulatable promoters of *Saccharomyces cerevisiae*: Comparison of transcriptional activity and their use for heterologous expression. *Nucl. Acids Res.* **22**, 5767–5768 (1994).
44. J. A. Lyons, A. Shahsavar, P. A. Paulsen, B. P. Pedersen, P. Nissen, Expression strategies for structural studies of eukaryotic membrane proteins. *Curr. Opin. Struct. Biol.* **38**, 137–144 (2016).
45. A. Punjani, J. L. Rubinstein, D. J. Fleet, M. A. Brubaker, cryoSPARC: Algorithms for rapid unsupervised cryo-EM structure determination. *Nat. Methods* **14**, 290–296 (2017).
46. E. F. Pettersen *et al.*, UCSF Chimera–A visualization system for exploratory research and analysis. *J. Comput. Chem.* **25**, 1605–1612 (2004).
47. L. G. Trabuco, E. Villa, K. Mitra, J. Frank, K. Schulten, Flexible fitting of atomic structures into electron microscopy maps using molecular dynamics. *Structure* **16**, 673–683 (2008).
48. R. T. Kidmose *et al.*, Namdinator–Automatic molecular dynamics flexible fitting of structural models into cryo-EM and crystallography experimental maps. *IUCrJ* **6**, 526–531 (2019).
49. A. Casanal, B. Lohkamp, P. Emsley, Current developments in Coot for macromolecular model building of electron cryo-microscopy and crystallographic data. *Protein Sci.* **29**, 1069–1078 (2020).
50. P. Emsley, B. Lohkamp, W. G. Scott, K. Cowtan, Features and development of Coot. *Acta Crystallogr. D, Biol. Crystallogr.* **66**, 486–501 (2010).
51. N. W. Moriarty, R. W. Grosse-Kunstleve, P. D. Adams, Electronic ligand builder and optimization workbench (eLBOW): A tool for ligand coordinate and restraint generation. *Acta Crystallogr. D, Biol Crystallogr.* **65**, 1074–1080 (2009).
52. P. D. Adams *et al.*, PHENIX: A comprehensive Python-based system for macromolecular structure solution. *Acta Crystallogr. D, Biol. Crystallogr.* **66**, 213–221 (2010).
53. P. V. Afonine *et al.*, Real-space refinement in PHENIX for cryo-EM and crystallography. *Acta Crystallogr. D, Struct. Biol.* **74**, 531–544 (2018).
54. V. B. Chen *et al.*, MolProbity: All-atom structure validation for macromolecular crystallography. *Acta Crystallogr. D, Biol. Crystallogr.* **66**, 12–21 (2010).

55. M. G. Prisant, C. J. Williams, V. B. Chen, J. S. Richardson, D. C. Richardson, New tools in MolProbity validation: CaBLAM for CryoEM backbone, UnDowser to rethink "waters," and NGL Viewer to recapture online 3D graphics. *Protein Sci.* **29**, 315–329 (2020).
56. O. V. Sobolev *et al.*, A global Ramachandran score identifies protein structures with unlikely stereochemistry. *Structure* **28**, 1249–1258.e1242 (2020).
57. S. Gore *et al.*, Validation of structures in the protein data bank. *Structure* **25**, 1916–1927 (2017).
58. A. Jurcik *et al.*, CAVER Analyst 2.0: Analysis and visualization of channels and tunnels in protein structures and molecular dynamics trajectories. *Bioinformatics* **34**, 3586–3588 (2018).
59. E. F. Pettersen *et al.*, UCSF ChimeraX: Structure visualization for researchers, educators, and developers. *Protein Sci.* **30**, 70–82 (2021).
60. J. Pei, B. H. Kim, N. V. Grishin, PROMALS3D: A tool for multiple protein sequence and structure alignments. *Nucl. Acids Res.* **36**, 2295–2300 (2008).
61. C. S. Bond, A. W. Schuttelkopf, ALINE: A WYSIWYG protein-sequence alignment editor for publication-quality alignments. *Acta Crystallogr. D, Biol. Crystallogr.* **65**, 510–512 (2009).
62. K. M. Frain *et al.*, S. cerevisia Niemann-Pick type C protein NCR1 in GDN at pH 7.5. Worldwide Protein Data Bank. https://doi.org/10.2210/pdb8qeb/pdb. Accessed 31 August 2023.
63. K. M. Frain *et al.*, S. cerevisia Niemann-Pick type C protein NCR1 in GDN at pH 5.5. Worldwide Protein Data Bank. https://doi.org/10.2210/pdb8qec/pdb. Accessed 31 August 2023.
64. K. M. Frain *et al.*, S. cerevisia Niemann-Pick type C protein NCR1 in LMNG at pH 5.5. Worldwide Protein Data Bank. https://doi.org/10.2210/pdb8qed/pdb. Accessed 31 August 2023.
65. K. M. Frain *et al.*, S. cerevisia Niemann-Pick type C protein NCR1 in Peptidisc at pH 7.5. Worldwide Protein Data Bank. https://doi.org/10.2210/pdb8qee/pdb. Accessed 31 August 2023.